

Correlations between the Hurst exponent and the maximal Lyapunov exponent for some low-dimensional discrete conservative dynamical systems

Mariusz Tarnopolski

Received: date / Accepted: date

Abstract The Chirikov standard map and the 2D Froeschlé map are investigated. A few thousand values of the Hurst exponent (HE) and the maximal Lyapunov exponent (mLE) are plotted in a mixed space of the nonlinear parameter versus the initial condition. Both characteristic exponents reveal remarkably similar structures in the mixed space. Moreover, a tight correlation between the HEs and mLEs for the two maps was found: $r_S = 0.83$ and $r_S = 0.75$ for the Chirikov and Froeschlé maps, respectively, where r_S is the Spearman rank. This correlation is remarkable, as the two exponents are descriptors of different features: the mLE is a measure of sensitivity to initial conditions, interconnected with chaos, and the HE is a measure of persistency, or long-term memory—it characterizes the incremental trend in the data. Based on this relation, a machine learning (ML) procedure, using the nearest neighbour algorithm, was performed to reproduce the HE distributions based on the mLE distributions. A few thousand points from the mixed spaces were used for the training, and then using $2 - 2.4 \times 10^5$ mLEs, the HEs were retrieved. The ML procedure allowed to reproduce the structure of the mixed spaces in great detail. The HE is proposed as an informative parameter in the area of chaotic control, as it provides expectations about the general trend in a time series.

Keywords Conservative Systems · Maximal Lyapunov Exponent · Hurst Exponent · Machine Learning

PACS 05.45.Ac · 05.45.Pq · 05.45.Tp · 05.40.Fb

Mariusz Tarnopolski
Astronomical Observatory
Jagiellonian University
Orla 171, 30-244
Kraków, Poland
E-mail: mariusz.tarnopolski@uj.edu.pl

1 Introduction

Dynamical systems play a crucial role in the description of the physical reality, being applied in fields such as cosmology [68], astrophysics [49, 72], nuclear physics [39], environmental science [69], financial analysis [22], among others. In particular, nonlinear systems often exhibit chaotic behaviour [1, 52], e.g. Chirikov standard map [14, 34] being a discrete volume preserving 2D example, or Lorenz [35] and Hénon-Heiles [27] systems, being 3D dissipative and 4D conservative continuous systems, respectively. Continuously, new chaotic systems are being discovered [2, 71]. Conservative systems, being Hamiltonian [10, 36], exhibit a complicated mixture of chaotic and regular components in phase space and do not possess a strange attractor [24]. Moreover, a mixed space of parameter–initial condition pairs allows to properly trace the route to chaos via period doubling [42]. On the other hand, a question about inferring chaotic dynamics from a scalar time series was also raised and efficiently answered decades ago [26, 55, 70].

Time series may be, in general, described by their statistical properties. One of its descriptors is a Hurst exponent (HE) [29, 43, 44], which is a measure of persistency, or long-range memory (or lack of thereof) [37] that is widely used, e.g., in financial analyses [12] and Solar physics [62]. An HE, denoted H , related to persistent (long-term memory) processes is greater than $1/2$, while for anti-persistent (short-term memory) there is $H < 1/2$ (see Sect. 2.2 for a detailed description). HEs proved to be useful indicators of morphological type in astrophysical processes, too [40, 64]. Despite being inherently unpredictable in long run, classical chaotic time series stem from deterministic processes (in opposition to quantum chaos), therefore order is expected to underly their dynamics (e.g. strange attractors [1, 5, 13, 45, 52]). A common behaviour in a variety of chaotic systems is the occurrence of irregular transitions between chaotic oscillations with a mean substantially different from the mean in other regions of the time domain (see Fig. 1 for an illustration). This leads to a hypothesis that chaotic time series should yield an HE greater than 0.5 in these instances (persistent behaviour), and indeed it was reported in [62] that a chaotic solution of Lorenz system (such as the one displayed in Fig. 1) possesses an $H > 0.64$.

1.1 Indicators of chaos

The Lyapunov exponent (LE) [5, 7, 8, 10, 36, 51, 52, 61, 70] is a measure of the mean exponential divergence (or convergence) of two initially nearby orbits of a dynamical system in its phase space in a time limit of infinity (see Sect. 2.1 for a detailed description). In a d -dimensional system, there are d such LEs, λ_i , related to each direction. Having an infinitesimal displacement between two initially nearby orbits, $\mathbf{w} \in \mathbb{R}^d$, their exponential divergence in the i -th phase space direction is characterized by $\lambda_i > 0$, related to chaotic behaviour¹. The maximal LE (mLE), λ_1 , is the simplest to compute among the Lyapunov spectrum, and indicates chaos if $\lambda_1 > 0$. If the divergence is slower than exponential, or the trajectories converge, then $\lambda_1 \leq 0$, and the trajectory is regular.

¹ In fact it implies local instability and sensitivity to initial conditions.

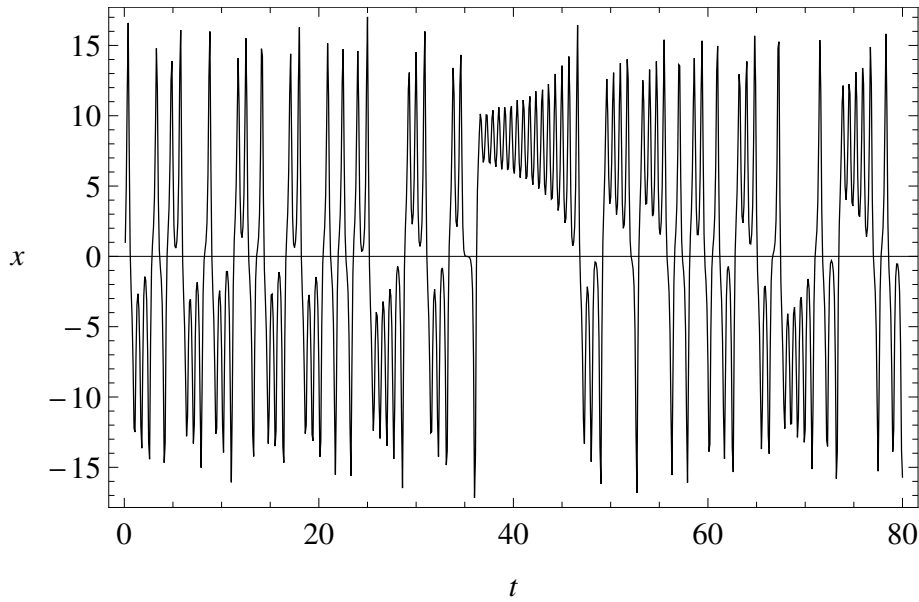


Fig. 1 The x component of the Lorenz equations $\dot{x} = \sigma(y - x)$, $\dot{y} = x(\rho - z) - y$, $\dot{z} = xy - \beta z$, with $\sigma = 10$, $\rho = 28$, $\beta = 8/3$, and initial condition $(x_0, y_0, z_0) = (1, 5, 10)$. There are regions where the time series keeps oscillating around some relatively high positive value (e.g. around $t \approx 40$), and where it stays at negative values for some time (e.g. around $t \approx 70$).

It is worth to mention that the mLE is not the only known indicator of chaos. In fact, several other indicators have been constructed, such as the fast Lyapunov indicator (FLI) [19, 20, 21], mean exponential growth factor of nearby orbits (MEGNO) [15, 16, 41]², smaller alignment index (SALI) [9, 10, 46, 59], the generalized alignment index (GALI) [10, 47, 48, 60], the relative Lyapunov indicator (RLI) [56, 57], or the rotation index [67], to mention only a few that rely on the solution of the variational equation (hence these methods are frequently called variational ones). In many aspects they have advantages over the conventional LEs as in many cases they are more sensitive and unambiguous in classifying an orbit (see e.g. [72, 73] for an application). Alternatively, there are diagnostics based on frequency decomposition (the frequency map analysis), in which the frequency vectors for various initial conditions form the frequency map, which is analysed by studying its regularity [31, 32, 33]. This method is conceptually different from the variational indicators as it does not employ the concept of divergence of nearby orbits. Finally, there is also a recent idea of the finite-time rotation number [63] as an indicator of chaos.

Nevertheless, the mLE still remains a valid indicator since it is quite easy to compute numerically and effective, especially when low-dimensional discrete maps are considered. Therefore, it will be explored in the remaining of this paper.

² There is a precise analytical relation between the FLI and MEGNO [50], due to which these two indicators are not independent.

1.2 Motivation

The research presented in this paper is primarily inspired by the findings in [62], where a time series analysis of the sunspot number was performed. The authors, for illustrative purposes, examined also a chaotic time series generated from the celebrated Lorenz equations [35] (see also Fig. 1), which resulted in an $H > 1/2$, indicating persistent behaviour. This leads to a question whether the properties of chaotic systems (mLE) are correlated to the long-term memory in the time series stemming from their dynamics (HE). Particularly, it is not that obvious that for chaotic orbits the related HE must always exceed $1/2$. Therefore, the correlations between the mLEs and HEs are to be examined herein.

The Chirikov standard map [14, 34] and the two-dimensional Froeschlé map³ [18] are chosen to work on (see Sect. 3 for a description). This choice is motivated by the simplicity of these maps, and also that (i) [42] provides an immediate comparison with the results obtained herein for the Chirikov standard map, and (ii) the 2D Froeschlé map has been also examined widely [18, 21, 59].

1.3 Aims and structure

In this work, correlations between mLEs and HEs are investigated for some 2D conservative maps: the Chirikov standard map [14] and the two-dimensional version of the Froeschlé map [18]. Machine learning (ML) is performed to effectively reproduce the statistical HE distribution given an mLE distribution, showing that the connection between these two allows to infer the HEs based on the mLEs only. A MATHEMATICA[®] v10.0.2 computer algebra system is used throughout.

This paper is organized in the following manner. In Sect. 2 the concepts of the mLE and HE are introduced, and the algorithms for their computation are described. In Sect. 3, the 2D maps under consideration are described, and the performance of the mLE and HE algorithms is demonstrated. The main results are presented in Sect. 4, which is followed by the ML approach in Sect. 5. Discussion and concluding remarks are gathered in Sect. 6.

2 Methods

The algorithms for the mLE and HE computation, described below, were implemented in MATHEMATICA[®], and the codes are presented in Appendix A.

2.1 Maximal Lyapunov Exponent (mLE)

Consider a discrete map M acting on an N -dimensional phase space vector \mathbf{y} ,

$$\mathbf{y}_{n+1} = M(\mathbf{y}_n), \quad (1)$$

³ Lacking an entrenched name, to differentiate from its well-studied 4-dimensional version, often termed the Froeschlé map, this 2D map is herein named the *2D Froeschlé map* as it first appeared in [18]. Note there are some naming ambiguities in the literature, e.g. in [28] the Chirikov standard map is called a Froeschlé map.

with $n = 0, 1, 2, \dots$, an initial condition \mathbf{y}_0 , and two initially nearby orbits (one of which is characterized by \mathbf{y}_0), displaced by an infinitesimal deviation vector \mathbf{w} , evolving with each iteration n according to a variational equation

$$\mathbf{w}_{n+1} = DM(\mathbf{y}_n) \cdot \mathbf{w}_n, \quad (2)$$

where $DM(\mathbf{y}_n)$ is the Jacobian matrix of the map M evaluated at \mathbf{y}_n . It follows from Eq. (2) that $\mathbf{w}_n = DM^n(\mathbf{y}_0) \cdot \mathbf{w}_0$, where

$$DM^n(\mathbf{y}_0) = DM(\mathbf{y}_{n-1}) \cdot DM(\mathbf{y}_{n-2}) \cdot \dots \cdot DM(\mathbf{y}_0). \quad (3)$$

Then, the LEs are given by [5, 7, 8, 10, 36, 51, 52, 61, 70]

$$\lambda_i = \lim_{n \rightarrow \infty} \frac{1}{n} \ln \frac{\|\mathbf{w}_n^i\|}{\|\mathbf{w}_0^i\|}, \quad (4)$$

where $i = 1, \dots, N$ corresponds to each orthogonal direction of the phase space. In practical implementations, the limit $n \rightarrow \infty$ is replaced by n sufficiently large, leading to the finite time LEs (FTLEs). Then, taking without loss of generality $\|\mathbf{w}_0^i\| = 1$, the LEs are approximated as [52]

$$\begin{aligned} \lambda_i &\simeq \frac{1}{n} \ln \|\mathbf{w}_n^i\| \\ &= \frac{1}{n} \ln \sqrt{[DM^n(\mathbf{y}_0) \cdot \mathbf{w}_0^i]^\top \cdot [DM^n(\mathbf{y}_0) \cdot \mathbf{w}_0^i]} \\ &\equiv \frac{1}{2n} \ln \left| (\mathbf{w}_0^i)^\top \cdot H_n(\mathbf{y}_0) \cdot \mathbf{w}_0^i \right| = \frac{1}{2n} \ln |h_i|, \end{aligned} \quad (5)$$

where h_i are the eigenvalues of the matrix $H_n(\mathbf{y}_0) = [DM^n(\mathbf{y}_0)]^\top DM^n(\mathbf{y}_0)$. When $n \rightarrow \infty$, FTLEs tend to the real values of LEs. Nevertheless, when n is finite but sufficiently large, the estimated maximal FTLE is a valid approximation of the mLE.

Let us denote the mLE by λ_1 , and order the LEs so that $\lambda_1 \geq \lambda_2 \geq \dots \geq \lambda_N$ (in fact, FTLEs will be used throughout this paper, but for simplicity, the notion mLE for λ_1 , obtained with Eq. (5), will be used hereinafter). If $\lambda_1 > 0$, then the considered orbit is chaotic, and regular otherwise. Note that $\lambda_1 = \max\{\lambda_i\}$, hence the mLE, being the dominant LE, is obtained using Eq. (5) on the dominant eigenvalue among $\{h_i\}_{i=1}^N$. It should be emphasized that it was explicitly assumed above that \mathbf{w}_0^i is an i -th eigenvector of the matrix $H_n(\mathbf{y}_0)$. In general, it may be a linear combination of the eigenvectors \mathbf{e}_j , $\mathbf{w}_0^i = \sum_{j=1}^N a_j^i \mathbf{e}_j$. Then, the deviation

$$\|\mathbf{w}_n^i\|^2 = \left| (\mathbf{w}_0^i)^\top \cdot H_n(\mathbf{y}_0) \cdot \mathbf{w}_0^i \right| = \sum_{j=1}^N a_j^2 \exp(2n\lambda_j), \text{ and for } n \text{ sufficiently large}$$

the sum is dominated by the largest exponent, corresponding to the mLE. For conservative maps with $N = 2$, there is $\lambda_1 + \lambda_2 = 0$, and hence knowing the mLE, the other LE is immediately accessible also [52].

2.2 Hurst Exponent (HE)

The HE, introduced by H. E. Hurst in 1951 [29] to model statistically the cycle of Nile floods, is a measure of long-term memory of a process (time series). It is closely related to the concept of a Brownian motion (Bm, or random walk) [43], for which

the consecutive increments are independent, and the standard deviation σ is scaled with step n as $\sigma \propto n^{1/2}$. Hurst found that in the case of Nile the increments were not independent, but characterized by a power law with an exponent greater than $1/2$. This leads to the fractional Brownian motion (fBm) [43], in which the system possesses a long-term memory (also called persistency), meaning that it somehow remembers its past increments and tends to maintain their trend. For instance, in a persistent process, if some measured quantity attains relatively high values, the system prefers to keep them high. This process is, however, probabilistic and hence at some point the observed quantity will eventually drop to oscillate around some relatively low value. But the process still has long-term memory, therefore it prefers to stay at those low values until the transition occurs again. The scaling of the standard deviation in such a process is $\sigma \propto n^H$, where H is the HE.

The HE can be also smaller than $1/2$ that corresponds to a Bm. In that case, the process is anti-persistent, and it possesses short-term memory, meaning that the observed values of some quantity frequently switch from relatively high to relatively low values, and there is no trend among the increments. The HE is also related to the autocorrelation of a time series, i.e. to the rate of its decrease with increasing lag. Hence, a persistent process with $H > 1/2$ is sometimes also called correlated, and an anti-persistent one, with $H < 1/2$, is called anti-correlated. Furthermore, the HE is bounded to the interval $(0, 1)$. The HE properties can be summarized as follows:

1. $0 < H < 1$,
2. $H = 1/2$ for a Bm (random walk),
3. $H > 1/2$ for a persistent (long-term memory, correlated) process,
4. $H < 1/2$ for an anti-persistent (short-term memory, anti-correlated) process.

Furthermore, the HE is related to a fractal dimension of a time series $D \in (1, 2)$ via $D = 2 - H$ [45]. This can be also generalized to $D > 2$ [13].

Among many existing computational algorithms for HE estimation (rescaled range, R/S [44], detrended fluctuation analysis [53, 54], wavelet approach [30, 58], to mention only a few), detrended moving average (DMA) [11] is used herein due to its simplicity and closed-form treatment [4]. In this method, first a moving average $\tilde{y}_n(i)$ of a time series $y(i)$ with equally spaced points $i = 1, 2, \dots, N_{\max}$, is computed:

$$\tilde{y}_n(i) = \frac{1}{n} \sum_{k=0}^{n-1} y(i-k), \quad (6)$$

i.e. the average of y for the last n data points, where $n \in [n_{\min}, n_{\max}]$ with a step of Δn . The moving average captures the trend of the signal over a (discretized) time interval n [66]. Next, the variance of $y(i)$ with respect to $\tilde{y}_n(i)$ is defined by

$$\sigma_{MA}^2 = \frac{1}{n_{\max} - n} \sum_{i=n}^{n_{\max}} [y(i) - \tilde{y}_n(i)]^2, \quad (7)$$

where $n_{\max} \ll N_{\max}$. Because it obeys the power law $\sigma_{MA} \propto n^H$, the HE is obtained as a slope of a linear regression in the $\log \sigma_{MA} - \log n$ plane.

3 Models

Two common conservative 2D systems are considered: the Chirikov standard map [14] and the 2D Froeschlé map [18]. Both are symplectic, governed by a single nonlinear parameter, and they exhibit, besides strictly regular and chaotic, also sticky behaviour.

3.1 Chirikov standard map

The Chirikov standard map in the form

$$\begin{cases} p_{n+1} = p_n + \frac{K}{2\pi} \sin(2\pi x_n), \\ x_{n+1} = x_n + p_{n+1}, \end{cases} \quad (8)$$

is examined. Its phase space portraits are displayed in Fig. 2 for a few values of the nonlinear parameter K . Global chaos occurs for $K > K_c \simeq 0.97163540631$ [23, 38]. The map can also exhibit sticky behaviour, which means that the orbit may look quite regular for some time and only after a sufficiently large number of iterations n its chaotic features start to be clearly visible (a transition from temporarily regular behaviour to apparently chaotic variations at some n_0 , i.e. the orbit might be easily misclassified if $N_{\max} \simeq n_0$). An example of such a situation is shown in Fig. 3. The mLE seems to slowly decrease to zero at first [convergence plots in Fig. 3 (a) and (c)], but at $n \approx 2500$ it suddenly starts to increase and plateau at a positive nonzero value. The stickiness is also clearly visible in the time series of p_n [Fig. 3 (e)], which looks very regular at first, but then starts to oscillate wildly. Contrary to this, the convergence plot of a regular orbit [Fig. 3 (b)] exhibits an n^{-1} decrease, clearly visible in a log-log plot [Fig. 3 (d)] as a straight line with slope equal to -1 , indicating that $\lambda_1 \rightarrow 0$ when $n \rightarrow \infty$. The time series of p_n is also completely regular for the whole range of n that it was iterated in (only a part is displayed in Fig. 3 (f) for the sake of clarity).

It was verified for some randomly chosen initial conditions and values of K that collecting the mLE after 10^4 iterations is sufficient for the purpose of this work. Moreover, in the estimation of the HE it was chosen to discard the first 4000 iterations due to a possibility of encountering sticky behaviour, i.e. for the DMA algorithm a time series of p_n with $n \in [4000, 10\,000]$ is used; p_n is employed as x_n is monotonic, hence yielding $H = 1$.

Having a time series of p_n , to obtain the HE according to Eq. (6) and (7) the following parameters are fixed and used throughout this paper: $n_{\min} = 10$, $n_{\max} = 300$, $\Delta n = 10$. Next, a linear regression is performed on the $\ln \sigma_{MA} - \ln n$ relation, and the slope of the fit is the HE. To confirm that the fitting is performed correctly, i.e. a line is fitted in the linear part of the plot, a number of statistical indicators are computed. First, the standard error of the slope is retrieved. Next, the end points (a, b) of the 99% confidence interval of the slope are used to calculate its width, $\alpha := b - a$. Finally, the Pearson coefficient R^2 is obtained. The standard deviation and α should be small compared to the HE obtained, and R^2 should be close to unity to conclude that the fitting was reliable.

An example of such an approach is illustrated in Fig. 4, in which case the results of the linear regression are as follows: $H = 0.4856$, the standard deviation is equal to 0.0047, $\alpha = 0.4985 - 0.4727 = 0.0258$, and $R^2 = 0.999$. This convincingly

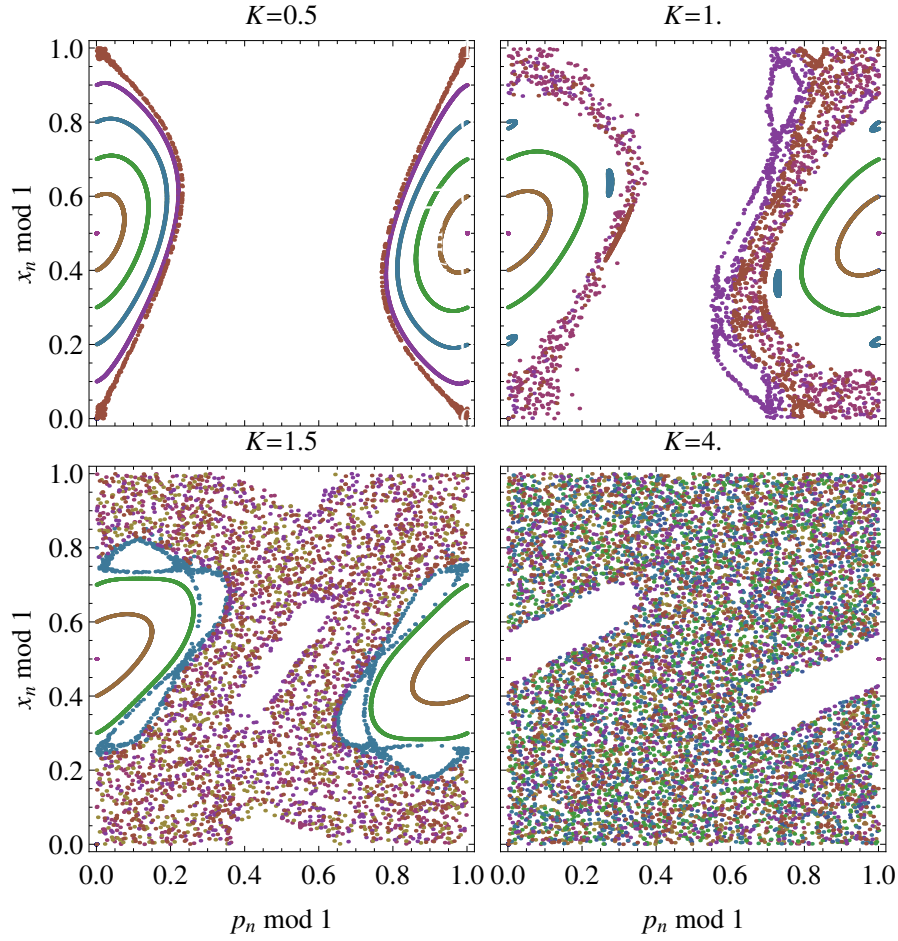


Fig. 2 (colour online) Phase space portraits of the folded (modulo 1 in both coordinates) Chirikov standard map for a few values of K . The initial conditions are $p_0 = 0.0$ and $x_0 \in [0.0, 1.0]$ with a step of 0.1. The map is iterated for 10^4 steps, and every tenth point is displayed in the plots.

places the HE slightly below the value of $1/2$ for this time series. It might happen, however, that some H exceeds unity, which is a meaningless result based on the mathematical theory (see Sect. 2.2), but is not surprising in numerical computations. Fortunately, it will turn out that these values are a negligible fraction in the statistic, and hence should not affect the main results and conclusions.

3.2 2D Froeschlé map

The 2D Froeschlé map in the form

$$\begin{cases} p_{n+1} = p_n - k \sin(x_n + p_n), \\ x_{n+1} = x_n + p_n, \end{cases} \quad (9)$$

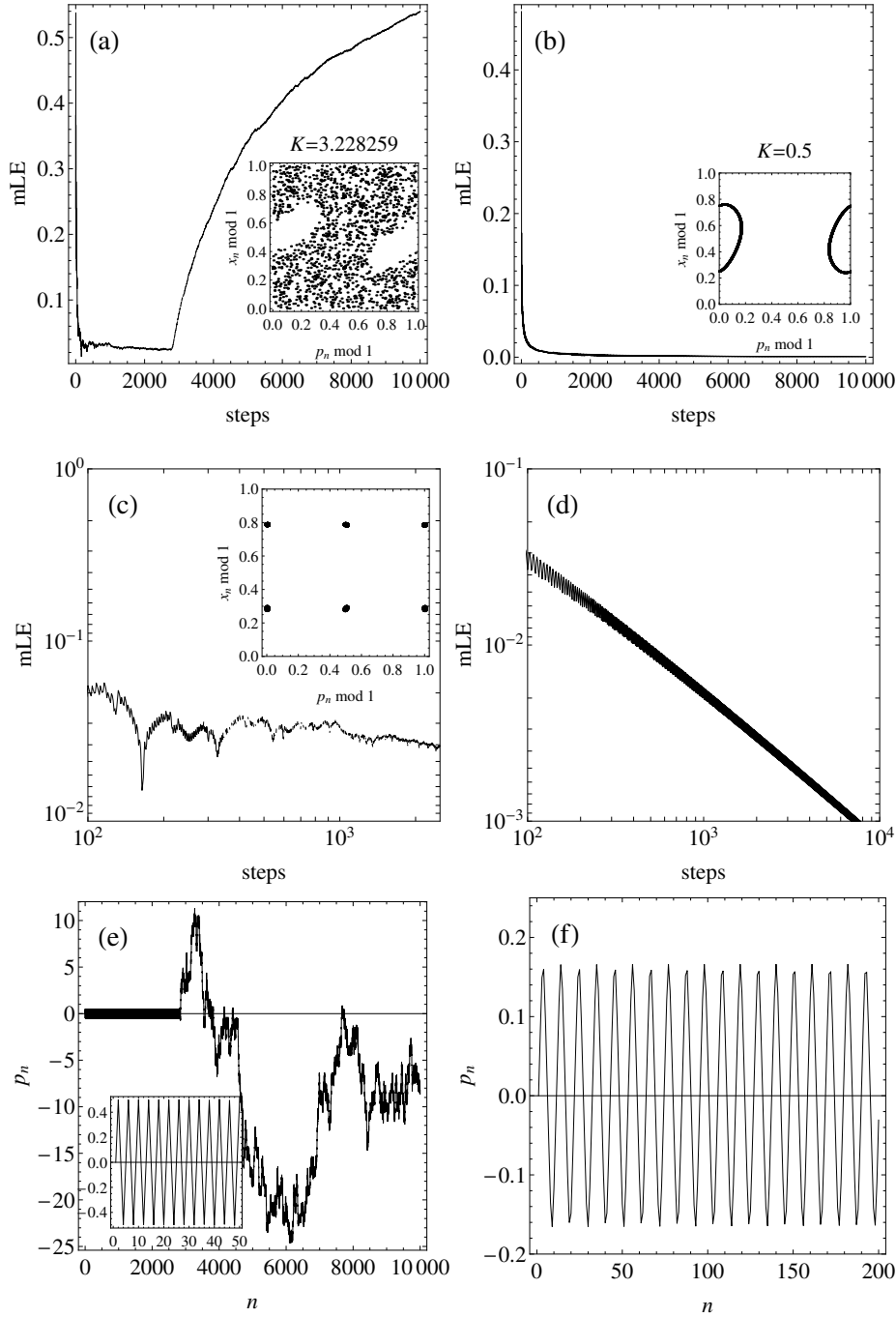


Fig. 3 Convergence plots of the mLE for (a) chaotic (which exhibits also sticky behaviour), with $(p_0, x_0) = (0.0, 0.2865)$, and (b) regular orbit, with $(p_0, x_0) = (0.0, 0.25)$. The insets show phase space portraits of the orbits. The map was iterated for 10^4 steps. (c) shows the log-log plot of the mLE convergence for the chaotic orbit in the region of sticky motion, i.e. up to 2500 steps. The inset shows the corresponding phase space portrait. (d) Shows the linear decline in case of the regular orbit. Note different scales in (c) and (d). In (e) the time series of p_n is displayed for the chaotic orbit; the inset shows its evolution for the first 50 iterations in the sticky region; (f) shows part of a p_n time series corresponding to a regular orbit.

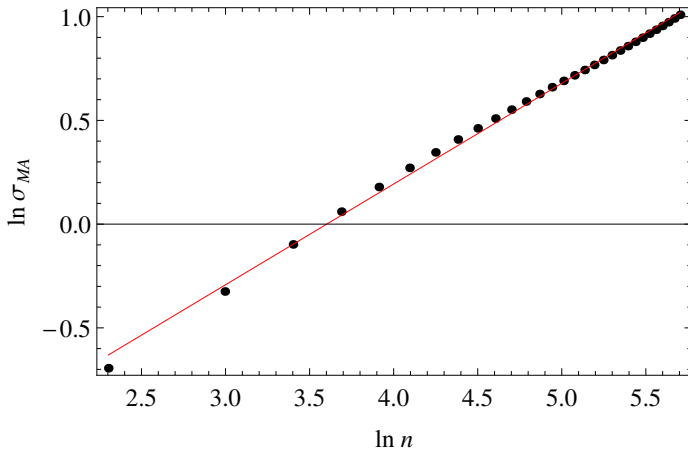


Fig. 4 (colour online) An example of HE estimation for the time series from Fig. 3 (e). See text for details.

is examined. It is formulated similarly to the map in Eq. (8), and belongs to the same family (it is sometimes also referred to as the standard map, though; see Footnote 3). Phase space portraits for a few values of k are displayed in Fig. 5. This map may also exhibit regular and chaotic motion; in particular, sticky behavior may be observed. Again, it was verified that 10^4 iterations are sufficient for the computation of the mLE, as it was for the Chirikov standard map, and in order to obtain the HEs, the first 4000 steps are discarded from the p_n time series (x_n is again monotonic), and its remaining part is the input of the DMA algorithm.

While it might happen for some orbits (in case of both the Chirikov and Froeschlé maps) that the total number of iterations, or the initial number of iterations discarded, will not be sufficient to skip over transient behaviour (e.g. stickiness), this should not be a concern, as several thousands of orbits are to be examined, and even if a small fraction will be misclassified, it should not affect the final results, which are of statistical character.

For completeness, it should be pointed that the computation of the HE using the DMA method was about 18 times more time-consuming than of the mLE for either of the maps.

4 Results

4.1 Chirikov standard map

A map of mLEs in a mixed space $K \times x_0$ on a grid of 101×51 points with $p_0 = 0.0$ is shown in Fig. 6(a). This is a recalculation of Fig. 2 in [42] but due to symmetry only non-negative x_0 's are taken into account. Although the overall picture sketched by both Figures (i.e., Fig. 6(a) and Fig. 2 in [42]) is consistent with each other, note slight differences in mLE values: according to [42], the biggest mLE attained in the $K \times x_0$ space is ≈ 1.2 , while herein the mLEs reach a value of ≈ 1.92 . The difference is caused by applying different algorithms: in [42] an mLE was extracted from a

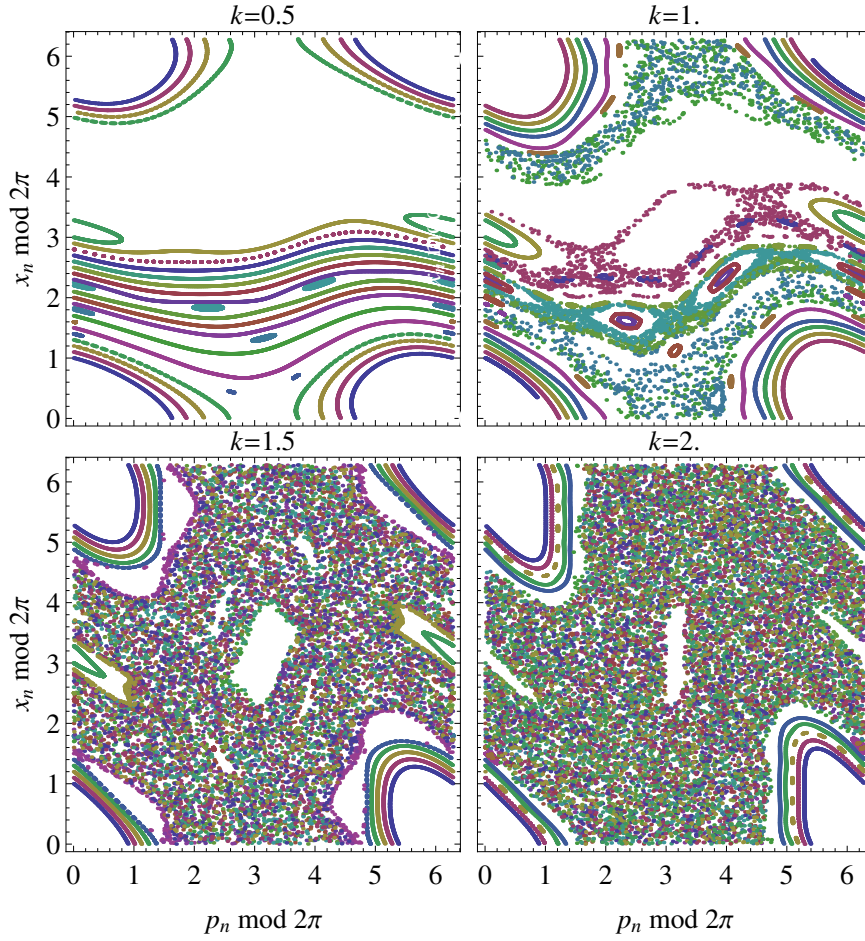


Fig. 5 (colour online) Phase space portraits of the folded (modulo 2π in both coordinates) 2D Froeschlé map for a few values of k . The initial conditions are $p_0 = 0.0$ and $x_0 \in [1.0, 3.0]$ with a step of 0.1. The map is iterated for 10^4 steps, and every tenth point is displayed in the plots.

timeseries as described by Wolf et al. [70] (Manchein, personal communication), while here the mLEs were computed according to the method described in Sect. 2.1 [52]. The difference is especially striking for the unstable line $x_0 = 0.0$, which is an exceptional line and it appears that the Wolf et al. method [70] could not fully grasp the underlying dynamics along this line.

Note also that in Fig. 6(a) some mLEs were undetermined (red points), because the eigenvalues of the matrix $[DM^n(\mathbf{y}_0)]^\top DM^n(\mathbf{y}_0)$ are zeros in some points, and the mLE is given according to Eq. (5) as their logarithm. Judging from the analysis in [42], the verification of the method performed in Sect. 3.1, and the relative difference between neighbouring (in the mixed space) mLEs, the division between regular and chaotic region is quite sharp. Because the mLEs are in fact FTLEs, because the limit in Eq. (4) is replaced by taking n sufficiently large (10^4

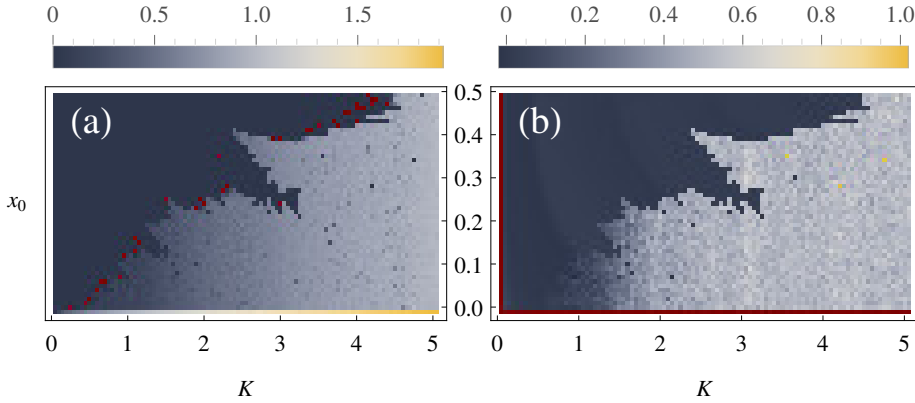


Fig. 6 (colour online) (a) mLEs and (b) HEs in the mixed space $K \times x_0$ with $p_0 = 0.0$ for Chirikov standard map, and a grid of $101 \times 51 = 5151$ points. Red points mark indeterminate values. Note different colour scales used.

iterations), they will in fact never converge to zero, and due to different convergence rates of different regular orbits, small-valued mLEs ($\sim 0.01 - 0.02$ in this work) are effectively ascribed to the regular domain. As this work is not focused on detailed aspects of the mixed space, already discussed in [42], but rather on general features—particularly, the differentiation between low and high mLEs is sufficient for the statistical analysis performed further on—the rich properties of the regular domain in the mixed space will not be discussed hereinafter⁴.

Next, a similar plot for HEs was drawn and is displayed in Fig. 6 (b). The unstable line $x_0 = 0.0$ had to be discarded as the HEs were undetermined by the algorithm. This is because, according to Eq. (8), the initial point $(0,0)$ is mapped also onto $(0,0)$ for all K , so the time series of p_n is constant, hence the DMA method leads to $\sigma_{MA} = 0$. If this is fed to the procedure of fitting a straight line in a log-log plot for the HE extraction described in Sect. 3.1, it results in indeterminate values. The same situation occurs for $K = 0$ and varying x_0 .

In Fig. 7 (a) the histograms of mLEs and HEs are displayed. The height of the peak around small mLE values is related to the size of the regular region in the mixed space, and the mLEs related to chaotic motion have a peak at $\sim 0.8 - 0.9$. In the HE distribution, there are two prominent peaks: one at small values, $H \sim 0$, and one located at H slightly exceeding $1/2$. Comparing this distribution with Fig. 6 (b), one may associate the two peaks with regular and chaotic domains of the mixed space, respectively.

Histograms in Fig. 7 (b) (standard deviation, range α of the 99% confidence interval, and Pearson's R^2 of each HE estimate) convince that the fitting procedure returned reliable estimates of HE values: the standard deviation of the slope does not exceed 0.03, and the Pearson R^2 does not fall below 0.9732. The range α of the confidence interval reaches a value as high as 0.164, but it has a mode of 0.02. Overall, the extracted HEs appear to be reasonable estimates.

⁴ The reader is referred to [42] for details regarding the interpretation of FTLEs in this context, and to [34] for a thorough analysis of the properties of the Chirikov standard map.

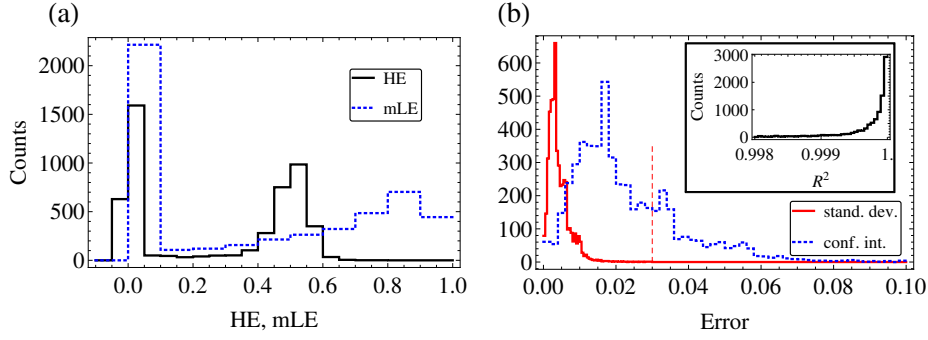


Fig. 7 (colour online) (a) Distributions of HEs and mLEs. Two distinct peaks are related to regular and chaotic domain of the mixed space. The mLE values greater than 1.0 are not displayed for the sake of clarity as they account for only 1.6% of all values, and are mainly located along the unstable line $x_0 = 0$. (b) HE errors; solid red – standard deviation, std, of the fitted slope, dashed blue – width of the 99% confidence interval, α . Maximal value of std is 0.03 (marked with a vertical red line), while α is not greater than 0.164. Inset shows the Pearson coefficient R^2 ; displayed bins contain 94% of counts. The minimal R^2 is 0.9732.

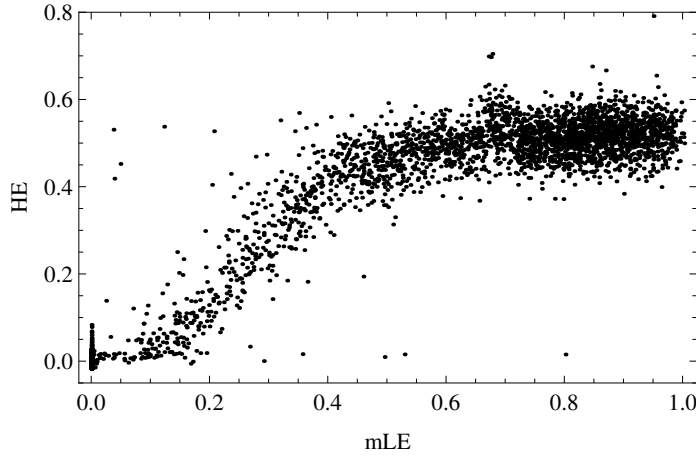


Fig. 8 Scatter plot for mLE–HE relation; $N_p = 4962$ points are displayed for which $r_S = 0.83$ and its p -value is numerically equal to zero.

After discarding outcomes being indeterminate for either mLE or HE, $N_p = 4962$ points with numerical values were left for which a scatter plot is shown in Fig. 8. The correlation is apparently nonlinear, hence a Spearman rank r_S is used to quantify its strength, and yielded $r_S = 0.83$, with p -values numerically equal to zero. Hence, the mLE–HE relation is a tight one.

Despite a negligible amount of outliers, the correlation between mLEs and HEs is very high, and as the computation of HEs took ~ 18 times longer than of mLEs, this relation will provide a useful insight into statistical distribution of HEs based on easier to compute mLEs.

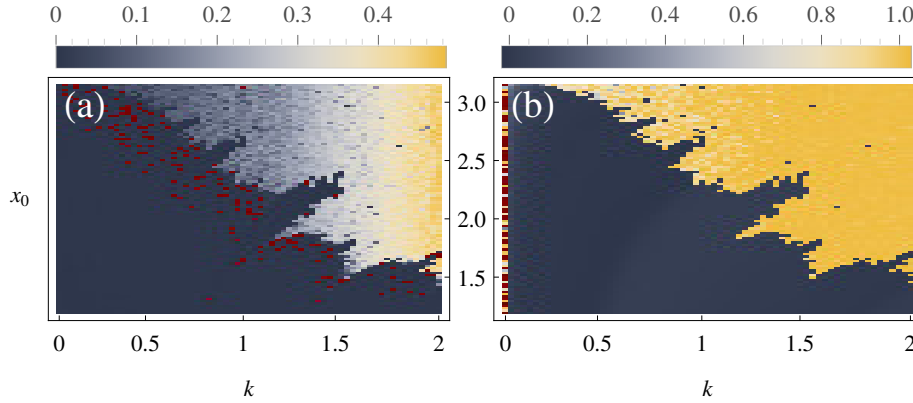


Fig. 9 (colour online) (a) mLEs and (b) HEs in the mixed space $k \times x_0$ with $p_0 = 0.0$ for a 2D Froeschlé map, and a grid of $67 \times 98 = 6566$ points. Red points mark indeterminate values. Note different colour scales used.

4.2 2D Froeschlé map

Next, the map given by Eq. (9) is investigated in the same manner as in the previous subsection. Figures 9(a) and (b) show the mLE and HE distributions, respectively, in the mixed space $k \times x_0$ with $p_0 = 0.0$, and exhibit the same structure as the Chirikov standard map does, i.e. bifurcating tongues of regular motion creeping in the chaotic zone. A significant difference is that the HEs gather around two extreme values, i.e. 0 for regular and 1 for chaotic regions, which is different than it was for the Chirikov standard map, and with a negligible gradient in between.

Statistical distributions, displayed in Fig. 10(a) (note a logarithmic scale for the ordinate), reveal an almost uniform distribution of mLEs for chaotic motion. Fittings performed for HE computation are not as reliable as in the former case, though. For example, the Pearson coefficient R^2 can attain a value as small as 0.0. On the other hand, a majority of fittings are characterized by errors small enough to allow examining at least general features of the HE distribution [compare with Fig. 10(b)]. Although the maximal 99% confidence interval range can be as wide as the whole theoretical range of HE values (spanning a unit interval from 0 to 1), the standard deviations do not exceed the value of 0.19, and (i) are centered around small absolute values, as indicated by the histogram in Fig. 10(b), and (ii) allow to distinguish chaotic from regular motions due to clearly separated peaks near extremal values of HEs.

Thus, as the scatter plot in Fig. 11 for this map does not possess as unambiguous structure as for the previous one, the distributions in Fig. 10 assure that the relation between mLEs and HEs is correctly grasped, at least at a first approximation. Note that the flat cut-off from above in Fig. 11 is a true feature and is not an artifact due to dropping indeterminate values (as $0 < H < 1$). Moreover, the higher the mLE, the smaller the scatter among corresponding HE values, and the critical mLE value, approximately at 0.04 (vertical dashed line in Fig. 11), sep-

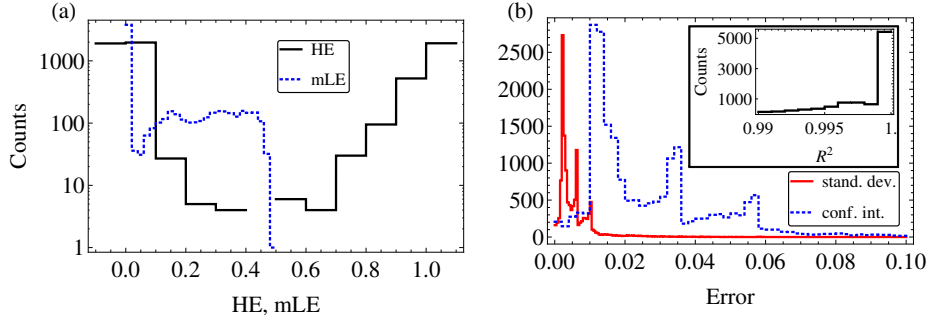


Fig. 10 (colour online) (a) Distributions of HE and mLE. Two distinct HE peaks are related to regular and chaotic domain of the mixed space. The mLE values are not greater than 0.5 and have an approximately uniform distribution inside the chaotic region. Note this is a semi-log plot. (b) HE errors; solid red – standard deviation, std, of the fitted slope, dashed blue – width of the 99% confidence interval, α . Maximal value of std is 0.19, while α spans an interval from 0 to 1.04. Inset shows the Pearson coefficient R^2 ; displayed bins contain 84% of counts. The minimal R^2 is 0. Extreme values of α and R^2 are rare enough to be treated as outliers.

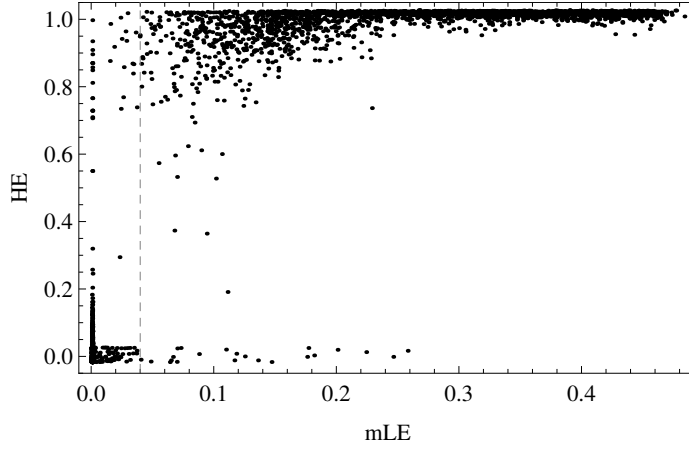


Fig. 11 Scatter plot for mLE–HE relation; $N_p = 6314$ points are displayed for which $r_S = 0.75$ and its p -value is numerically equal to zero.

arates accurately small HEs from larger ones, or equivalently in this case, values corresponding to regular and chaotic zones in the mixed space.

5 Machine learning

5.1 Method

In the previous Sect. 4, a correspondence between mLEs and HEs was found. They were computed in a given point in the mixed space $param \times x_0$, where $param$ is a nonlinear parameter, K or k in Eq. (8) and (9), respectively. Hence, we are equipped with pairs of three-dimensional vectors in the form $(param, x_0, mLE)$

and $(param, x_0, H)$, where the first two components of each vectors are the same for a given map, i.e. the mLEs and HEs were evaluated in the same points of the mixed space. Herein, a machine learning (ML) procedure is applied to those sets of vectors in order to predict HE values based only on the triples $(param, x_0, mLE)$. The aim of this approach is (i) to train a classifier on $\approx 5000 - 6000$ vector pairs from the previous Sect. 4, (ii) to compute a greater number of mLEs (i.e., in the mixed space with finer grid), resulting in $> 2 \times 10^5$ mLEs, and (iii) to use the trained classifier to infer the HE values based on the mLEs. For this purpose, the nearest neighbour (NN) [3, 6, 17, 25, 65] algorithm is employed, with an Euclidean metric to measure the distance. Its power lies in simplicity and accuracy. The training of an NN classifier is simply feeding it with the list of assignments $\{(param, x_0, mLE)_i \rightarrow HE_i\}_{i=1}^{i=N_p}$. Next, given a new mLE, not present in the training set, together with its location in the mixed space, its nearest neighbour is found among the triples $(param, x_0, mLE)$ that were used in the training process. The corresponding HE is ascribed to the new mLE. The ML is motivated by the tight correlation between the mLEs and HEs found for the Chirikov standard and 2D Froeschlé maps.⁵

5.2 Results

ML training on a set of assignments $\{(param, x_0, mLE)_i \rightarrow HE_i\}_{i=1}^{i=N_p}$ from Sect. 4 is performed, where N_p is an appropriate number of points used with respect to the map under consideration. The output are machine-learnt functions $p(x)$, whose input are the mLEs located in the mixed space, and their output is an HE related to the same point in the same space, evaluated using the NN algorithm. Next, $\approx 2.0 \cdot 10^5$ mLEs are produced for the Chirikov standard map on a grid of 1001×201 points in the mixed space $K \times x_0$, and similarly $\approx 2.4 \cdot 10^5$ mLEs on a grid of 501×486 points for the 2D Froeschlé map in the space of $k \times x_0$. Resultant mLE distributions are shown in Fig. 12(a) and (b), and are consistent with Fig. 7(a) and Fig. 10(a). For the Chirikov standard map two distinct peaks are easily distinguishable, while the distribution for the 2D Froeschlé map is nearly uniform for non-zero⁶ mLEs corresponding to chaotic motion, and with a steep decrease just before 0.5. Machine-learnt functions $p(x)$ were then applied and the HE distributions reproduced with their aid are displayed in Fig. 12(c) and (d). To emphasize that the underlying initial mLE distribution is crucial and $p(x)$ itself is not informative, HE distributions are computed also for artificial, uniform mLE distributions. This resulted in uniformly mapped, via $p(x)$, HE distributions, overlaid with the actual ones in Fig. 12(c) and (d), significantly different from the real ones, especially for the Chirikov standard map. The difference for the 2D Froeschlé map is visible in the height of the peak near zero-values, as the rest of the real distribution is almost uniform, hence not really different from the artificial one.

These machine-learnt HE distributions were eventually mapped on the mixed space and the results are shown in Fig. 12(e) and (f). Regular and chaotic regions

⁵ The described approach is implemented in MATHEMATICA[®] via a command `Predict` with `NearestNeighbors` chosen as the method of the ML. In fact, the training is a one-line code.

⁶ Non-zero meaning greater than 0.01 – 0.02, that are prescribed to the regular domain.

are sharply divided, as in Fig. 6 and Fig. 9, and the coverage appears to be nearly perfect. It is important to note that, e.g. for the Chirikov standard map, $p(x)$ is obtained only based on mLEs and HEs *both* determinate, i.e., as described in Sect. 4.1, extreme mLEs along the unstable line $x_0 = 0.0$ were discarded due to a lack of corresponding HEs. This is why the absolute colour functions in Fig. 6(b) and Fig. 12(e) are different, yet the relative shapes of the distributions are apparently nearly identical. The same applies for the 2D Froeschlé map in Fig. 9(b) and Fig. 12(f).

Finally, let us note that the mLE–HE relations displayed in the form of a scatter plot in Fig. 7 and 11, have common features: a plateau at approximately half of the largest attainable mLE and a steep increase before. Left part of the relations is obviously influenced by the amount of nearly-zero mLEs, which is approximately linearly dependent on the size of the regular zone relative to the chaotic region. This means that $p(x)$ may be different if the mixed space is bounded differently, therefore the HE distributions obtained with the aid of $p(x)$ will have the relative heights of the peaks dependent on the ratio of regular and chaotic orbits in the part of the mixed space examined. Nevertheless, as the mLE and HE distributions in the chaotic zones are not entirely characterized by a single peak, the inferred $p(x)$ is likely to describe the mLE–HE relations correctly.

6 Discussion and conclusions

It was suspected, based on the result of [62] for the Lorenz system [35] for which an $H > 1/2$ was computed, that chaotic time series might be generally characterized by an HE exceeding $1/2$, indicating persistent behaviour of the corresponding time series. The mLE and HE distributions were computed for two 2D conservative discrete maps, the Chirikov standard map [14] and the 2D Froeschlé map [18]. Both characteristic exponents reveal remarkably similar structures in the mixed space of nonlinear parameter versus initial condition (see Fig. 6 and 9). Moreover, a tight correlation between the HEs and mLEs for the two maps was found: $r_S = 0.83$ and $r_S = 0.75$ for the Chirikov and Froeschlé maps, respectively. This is remarkable, as the two exponents are descriptors of different behaviour: the mLE is a measure of sensitivity to initial conditions, interconnected with chaos, and the HE is a measure of persistency (long-term memory, autocorrelation)—it characterizes the incremental trend in the data.

In case of the 2D Froeschlé map (Sect. 4.2) the HEs tend to gather at $H \sim 0$ in case of regular, and at $H \sim 1$ in case of chaotic motion. The HE distribution is characterized by two sharp peaks [Fig. 10 (a)]. The Chirikov standard map (Sect. 4.1) yielded more interesting results: while regular motion again corresponds to $H \sim 0$, the HE peak related to the chaotic zone is at $H = 0.4 - 0.6$, and with a steady gradient in between (Fig. 7 (a) and 8). This is a somewhat different result that was expected based on the Lorenz system, however, it is a continuous dissipative system, contrary to the systems examined herein, which are conservative and discrete.

Motivated by the tight correlation between the mLEs and HEs, an ML procedure, using the NN algorithm, was performed to reproduce the HE distributions based on the mLE distributions (Sect. 5). Approximately 5000 – 6000 points from the mixed spaces were used for the training, and then using $2 - 2.4 \times 10^5$ mLEs,

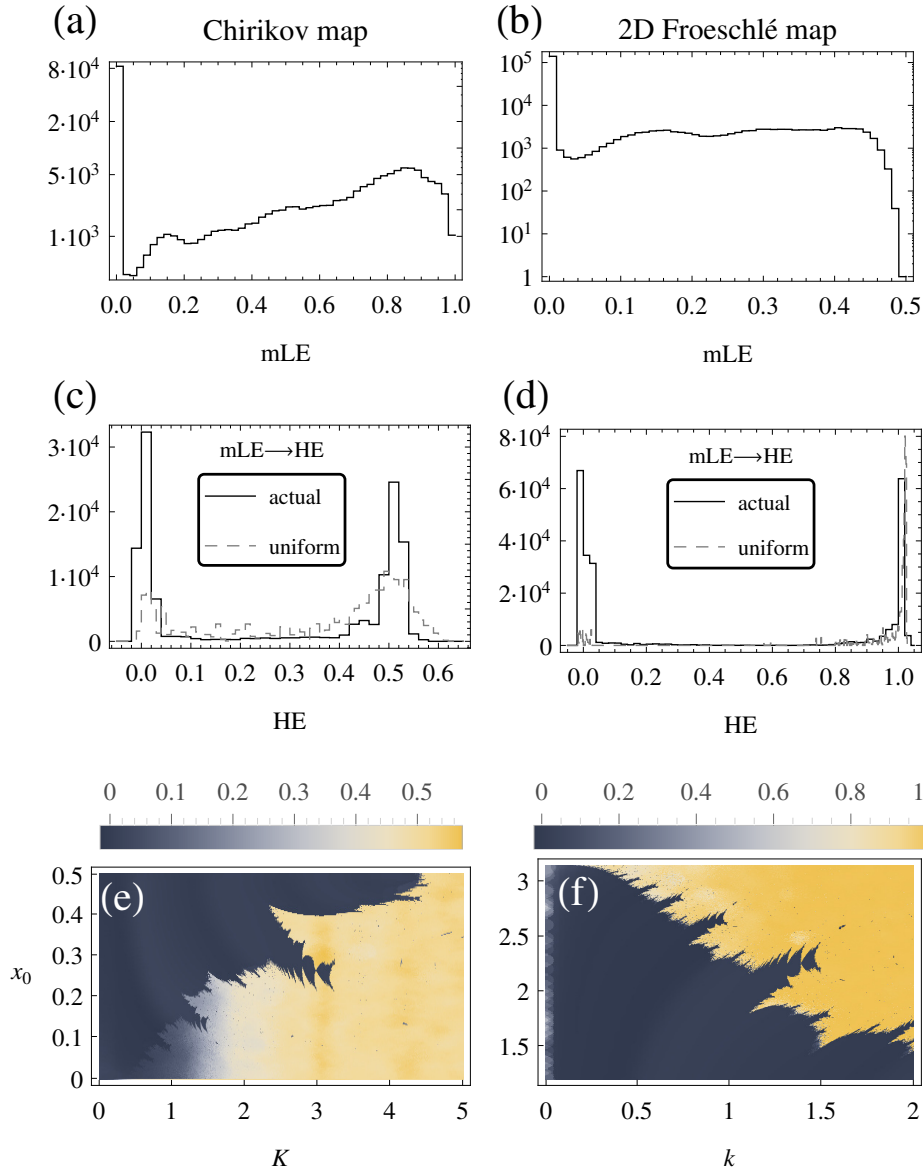


Fig. 12 (colour online) *Left column:* Chirikov standard map. *Right column:* 2D Froeschlé map. (a)—(b) Actual mLE distributions for $\approx 2.0 \cdot 10^5$ and $2.4 \cdot 10^5$ values, respectively. (c)—(d) HE distributions obtained by the machine-learned function $p(x)$ with an NN method; solid black — actual distributions obtained by applying $p(x)$ to (a) and (b); dashed gray — comparison distributions obtained by applying $p(x)$ to artificial uniform distributions (at the level of ≈ 5000). (e)—(f) HE distributions in the mixed space reproduced by applying appropriate $p(x)$ to (a) and (b). Note different colour scales used.

the HEs were retrieved. It should be emphasized that the shape of the mLE–HE relation is crucial here, as when an artificially, uniformly distributed set of mLEs was used, the retrieved HE distributions were different than the ones computed directly from the time series [Fig. 12 (c)—(d)]. The NN procedure, applied to the true mLEs, allowed to reproduce the structure of the mixed spaces in great detail [Fig. 12 (e)—(f)].

To conclude, the important results obtained in this work are as follows:

1. For the low-dimensional conservative maps examined herein, i.e. the Chirikov standard map and the 2D Froeschlé map, the mLEs and HEs were found to be highly correlated, and the correlations are positive.
2. For both maps, the HEs corresponding to chaotic motion are systematically higher than the ones related to regular motion.
3. In case of the Chirikov standard map, the chaotic zone is described by HEs in the range $\sim 0.4 - 0.6$, while for the 2D Froeschlé map chaos was characterized by $H \sim 1$. In both cases, regular motion yields $H \sim 0$.
4. Based on the correlations obtained, an ML was performed, and its results, applied to a much greater number of mLEs, allowed to reproduce the structure of the mixed spaces in great details, including the bifurcating tongues.
5. Finally, the HE appears to be an informative parameter, that might find its place in the field of chaotic control, as it gives expectations about the general trend in the time series.

The cause underlying the mLE–HE relations, however, as well as the differences between the two maps, remains an open issue. Moreover, a question about its shape for different types of systems (non-symplectic, dissipative, higher dimensional, continuous, hyperchaotic, etc.) naturally arises. It is believed that further exploration of this topic will lead to a deeper understanding of chaotic dynamical systems.

Acknowledgements The author wishes to express his gratitude to the anonymous referees whose useful comments lead to significant improvements in the quality of the paper.

A Appendix: Codes for computing the mLE and HE

The MATHEMATICA[®] code for calculating the mLE of the Chirikov standard map given by Eq. (8) is:

```
mLE[init_List, param_, nmax_] := mLE[init, param, nmax] =
Block[{G, JacobianMatrix, DF, p, x, vals, DFs, v, DFnTbl},
  G[{p_, x_}] := G[{p, x}] = {p + param/(2 \[Pi]) Sin[2 \[Pi] x], x + p + param/(2 \[Pi]) Sin[2 \[Pi] x]};
  JacobianMatrix[funs_List, vars_List] := JacobianMatrix[funs, vars] = Outer[D, funs, vars];
  DF[n_] := DF[n] = JacobianMatrix[G[{p, x}], {p, x}] /. {p -> vals[[n, 1]], x -> vals[[n, 2]]};
  vals = NestList[G, init, nmax - 1];
  DFs = Reverse[Table[DF[n], {n, 1, nmax}]];
  v[1] = Last[DFs];
  v[n_] := v[n] = DFs[[Length[DFs] - (n - 2)]];
  DFnTbl = Table[v[i], {i, 1, nmax}];
  {1./(2 nmax) Max[Log[Abs[Eigenvalues[Transpose[Last[DFnTbl]]. Last[DFnTbl]]]], vals]}
```

where `init` is an initial condition, `param` is the nonlinear parameter K , and `nmax` is the number of iterations. For example, to compute the mLE of the chaotic orbit in Fig. 3 (a) after 10000 iterations: `mLE[{0.0, 0.2865}, 3.228259, 10000]`.

To compute the mLE of the 2D Froeschlé map given by Eq. (9), it is sufficient to replace the definition of `G[{p, x}]` using `{p + x, x - param Sin[p + x]}`. This code is general enough to work for a map of any dimension with an arbitrary number of parameters (thence, in the definition of the `mLE` function, `param` should be an appropriate list of parameters).

The code for computing the HE of the Chirikov standard map is:

```
Hurst[ init_ , param_ , ndisc_ , nmax_ , Hnmin_ , Hnmax_ , Hnstep_ ] :=
Hurst[ init , param , ndisc , nmax , Hnmin , Hnmax , Hnstep ] =
Block[{G, vals , y , ytilde , sigma , out , log , hurst , fit , nlm , A , B , z },
  G[{p_ , x_}] := G[{p, x}] = {p + param/(2 \[Pi]) Sin[2 \[Pi] x], x + p + param/(2 \[Pi]) Sin[2 \[Pi] x]};
  vals = NestList[G, init , nmax - 1];
  y = Table[vals[[i, 1]], {i, ndisc , Length[vals ]}];
  ytilde[n_ , i_ ] := ytilde[n, i] = \!(\(*UnderoverscriptBox[\(\[Sum]\), \((k = 0\), \((n - 1\))\)(y[[i - k]])\)/n;
  sigma[n_ ] := sigma[n] = Sqrt[\!(\(*UnderoverscriptBox[\(\[Sum]\), \((i = n\), \((Length[y ])\)*SuperscriptBox[\((y[[i]] - ytilde[n, i])\), \((2\))\)]/((Length[y] - n));
  out = Table[sigma[n], {n, Hnmin , Hnmax , Hnstep}];
  log = Table[Log[i], {i, N[Hnmin], N[Hnmax], N[Hnstep]}];
  hurst = Table[Log[out[[i ]]], {i, 1, Length[out]}];
  fit = Table[{log[[i ]], hurst[[i ]], {i, 1, Length[log]}];
  nlm = NonlinearModelFit[fit , A z + B , {A , B}, z];
  {Normal[nlm][[2, 1]], nlm["ParameterErrors" ][[1]], nlm["ParameterConfidenceIntervals" , ConfidenceLevel -> 0.99][[1]], nlm["RSquared"]}]
```

where `Hnmin`, `Hnmax` and `Hnstep` are n_{\min} , n_{\max} and Δn , respectively, defining the region where the $\sigma_{MA} - n$ relation should be established, and `ndisc` is the number of iterations to be discarded from the time series. For example, to compute the HE of the chaotic orbit in Fig. 3 (a): `Hurst[{0.0, 0.2865}, 3.228259, 4000, 10000, 10, 300, 10]`.

The same code was used for the 2D Froschlé map, after replacing the definition of `G[{p, x}]` appropriately. For other maps, fiddling with the parameters may be required.

References

1. Alligood, K. T., Sauer, T. D., Yorke, J. A.: *Chaos: an Introduction to Dynamical Systems*, Springer New York (2000)
2. Alpar, O.: Analysis of a new simple one dimensional chaotic map. *Nonlinear Dyn.* **78**(2), 771–778 (2014)
3. Altman, N. S.: *An Introduction to Kernel and Nearest-Neighbor Nonparametric Regression*. *Am. Stat.* **46**, 175–185 (1992)
4. Arianos, S., Carbone A.: Detrending moving average algorithm: A closed-form approximation of the scaling law. *Physica A* **382**, 9–15 (2007)
5. Baker, G., Gollub, J.: *Chaotic Dynamics: An Introduction*. Cambridge University Press, 2nd edition (1996)
6. Barber, B.: *Bayesian Reasoning and Machine Learning*. Cambridge University Press (2012)
7. Benettin, G., Galgani, L., Giorgilli, A., Strelcyn, J.-M.: Lyapunov characteristic exponents for smooth dynamical systems and for Hamiltonian systems; a method of computing all of them. Part 1: Theory. *Meccanica* **15**, 9–20 (1980)
8. Benettin, G., Galgani, L., Giorgilli, A., Strelcyn, J.-M.: Lyapunov characteristic exponents for smooth dynamical systems and for Hamiltonian systems; a method of computing all of them. Part 2: Numerical application. *Meccanica* **15**, 21–30 (1980)
9. Bountis, T., Skokos, Ch.: Application of the SALI chaos detection method to accelerator mappings. *Nucl. Instr. Meth. Phys. Res. Sect. A* **561**(2), 173–179 (2006)
10. Bountis, T., Skokos, H.: *Complex Hamiltonian Dynamics*, Springer Berlin Heidelberg (2012)

11. Alessio, E., Carbone, A., Castelli, G., Frappietro, V.: Second-order moving average and scaling of stochastic time series. *Eur. Phys. J. B* **27**(2), 197–200 (2002)
12. Carbone, A., Castelli, G., Stanley, H. E.: Time-dependent Hurst exponent in financial time series. *Physica A* **344**(1–2), 267–271 (2004)
13. Carbone, A.: Algorithm to estimate the Hurst exponent of high-dimensional fractals. *Phys. Rev. E* **76**, 056703 (2007)
14. Chirikov, B. V.: A universal instability of many-dimensional oscillator systems. *Phys. Rep.* **52**(5), 263–379 (1979)
15. Cincotta P. M., Simó C.: Simple tools to study global dynamics in non-axisymmetric galactic potentials - I. *Astronomy and Astrophysics Supplement* **147**, 205–228 (2000)
16. Cincotta P. M., Giordano C. M., Simó C.: Phase space structure of multi-dimensional systems by means of the mean exponential growth factor of nearby orbits. *Physica D* **182**(3–4), 151–178 (2003)
17. Cover, T. M., Hart, P. E.: Nearest Neighbor Pattern Classification. *IEEE Trans. Inform. Theory*, **IT-13**, 21–27 (1967)
18. Froeschlé, C.: On the number of isolating integrals in systems with three degrees of freedom. *Astrophys. Space Sci.* **14**(1), 110–117 (1971)
19. Froeschlé C., Gonczi R., Lega E.: The fast Lyapunov indicator: a simple tool to detect weak chaos. Application to the structure of the main asteroidal belt. *Planet. Space Sci.* **45**(7), 881–886 (1997a)
20. Froeschlé C., Lega E., Gonczi R.: Fast Lyapunov Indicators. Application to Asteroidal Motion. *Cel. Mech. Dyn. Astron.* **67**(1), 41–62 (1997b)
21. Froeschlé C., Lega E.: On the Structure of Symplectic Mappings. The Fast Lyapunov Indicator: a Very Sensitive Tool. *Cel. Mech. Dyn. Astron.* **78**(1), 167–195 (2000)
22. Gao, Q., Ma, J.: Chaos and Hopf bifurcation of a finance system. *Nonlinear Dyn.* **58**(1–2), 209–216 (2009)
23. Greene, J. M.: A method for determining a stochastic transition. *J. Math. Phys.* **20**(6), 1183–1201 (1979)
24. Greiner, W.: *Classical Mechanics. Systems of Particles and Hamiltonian Dynamics*. Springer Berlin Heidelberg (2010)
25. Hastie, T., Tibshirani, R., Friedman, J.: *The Elements of Statistical Learning*. Springer, 2nd edition (2009)
26. Hegger, R., Kantz, H., Schreiber, T.: Practical implementation of nonlinear time series methods: The TISEAN package. *Chaos* **9**(2), 413–435 (1999)
27. Hénon, M., Heiles, C.: The applicability of the third integral of motion: some numerical experiments. *Astron. J.* **69**(1), 73–79 (1964)
28. Howard, J. E., Dullin, H. R.: Linear stability of natural symplectic maps. *Phys. Lett. A* **246**(3–4), 273–283 (1998)
29. Hurst, H. E.: Long-term storage capacity of reservoirs. *Trans. Am. Soc. Civ. Eng.* **116**, 770–799 (1951)
30. Jones, C. L., Lonergan, G. T., Mainwaring, D. E.: Wavelet packet computation of the Hurst exponent. *J. Phys. A* **29**(10), 2509–2527 (1996)
31. Laskar, J.: The chaotic motion of the solar system - A numerical estimate of the size of the chaotic zones. *Icarus* **88**, 266–291 (1990)
32. Laskar, J., Froeschlé, C., Celletti, A.: The measure of chaos by the numerical analysis of the fundamental frequencies. Application to the standard mapping. *Physica D* **56**(2–3), 253–269 (1992)
33. Laskar, J.: Frequency analysis for multi-dimensional systems. Global dynamics and diffusion. *Physica D* **67**(1–3), 257–281 (1993)
34. Lichtenberg, A. J., Leiberman, M. A.: *Regular and Chaotic Dynamics*. Springer-Verlag (1992)
35. Lorenz, E. N.: Deterministic Nonperiodic Flow, *J. Atmos. Sci.* **20**(2), 130–141 (1963)
36. Lowenstein, J. H.: *Essentials of Hamiltonian Dynamics*. Cambridge University Press (2012)
37. Machado, J. A. T., Lopes, A. M.: The Persistence of Memory. *Nonlinear Dyn.* (2014) doi:10.1007/s11071-014-1645-1
38. MacKay, R. S.: A renormalization approach to invariant circles in area-preserving maps. *Physica D* **7**(1–3), 283–300 (1983)
39. MacKay, R. S., Meiss, J. D. (Eds.): *Hamiltonian Dynamical Systems: A Reprint Selection*. CRC Press (1987)
40. MacLachlan, G. A., Shenoy, A., Sonbas, E., Coyne, R., Dhuga, K. S., Eskandarian, A., Maximon, L. C., Parke, W. C.: The Hurst exponent of Fermi gamma-ray bursts. *Mont. Not. R. Astron. Soc.* **436**(4), 2907–2914 (2013)

41. Maffione, N. P., Giordano, C. M., Cincotta, P. M.: Testing a fast dynamical indicator: The MEGNO. *Int. J. Non-Linear Mech.* **46**(1), 23–34 (2011)
42. Manchein, C., Beims, M. W.: Conservative Generalized Bifurcation Diagrams. *Phys. Lett. A* **377**(10–11), 789–793 (2013)
43. Mandelbrot, B. B., van Ness, J. W.: Fractional Brownian Motion, Fractional Noises and Applications. *SIAM Rev.* **10**, 422–437 (1968)
44. Mandelbrot, B. B., Wallis, J. R.: Noah, Joseph, and Operational Hydrology. *Water Resour. Res.* **4**(5), 909–918 (1969)
45. Mandelbrot, B. B.: *Fractal Geometry of Nature*. W. H. Freeman & Company (1983)
46. Manos, T., Skokos, Ch., Athanassoula, E., Bountis, T.: Studying the global dynamics of conservative dynamical systems using the SALI chaos detection method. *Nonlin. Phenom. Complex Syst.* **11**, 171–176 (2008)
47. Manos, T., Skokos, Ch., Antonopoulos, Ch.: Probing the Local Dynamics Of Periodic Orbits by the Generalized Alignment Index (GALI) Method. *Int. J. Bif. Chaos* **22**(9), 250218 (2012)
48. Manos, T., Bountis, T., Skokos, Ch.: Interplay between chaotic and regular motion in a time-dependent barred galaxy model. *J. Phys. A* **46**(25), 254017 (2013)
49. Manos, T., Machado, R. E. G.: Chaos and dynamical trends in barred galaxies: bridging the gap between N -body simulations and time-dependent analytical models. *Mont. Not. R. Astron. Soc.* **438**(3), 2201–2217 (2014)
50. Mestre, M. F., Cincotta, P. M., Giordano, C. M.: Analytical relation between two chaos indicators: FLI and MEGNO. *Mont. Not. R. Astron. Soc.* **414**(1), L100–L103 (2011)
51. Oseledec, V. I.: A multiplicative ergodic theorem. Lyapunov characteristic numbers for dynamical systems. *Trans. Mosc. Math. Soc.* **19**, 197–231 (1968)
52. Ott, E.: *Chaos in Dynamical Systems*. Cambridge University Press (2002)
53. Peng, C.-K., Buldyrev, S. V., Havlin, S., Simons, M., Stanley, H. E., Goldberger A. L.: Mosaic organization of DNA nucleotides. *Phys. Rev. E* **49**(2), 1685–1698 (1994)
54. Peng, C.-K., Havlin, S., Stanley, H., Goldberger, A. L.: Quantification of scaling exponents and crossover phenomena in nonstationary heartbeat time series. *Chaos* **5**(1), 82–87 (1995)
55. Rosenstein, M. T., Collins, J. J., De Luca, C. J.: A practical method for calculating largest Lyapunov exponents from small data sets. *Physica D*, **65**(1–2), 117–134 (1993)
56. Sándor, Z., Érdi, B., Efthymiopoulos, Ch.: The Phase Space Structure Around L4 in the Restricted Three-Body Problem. *Cel. Mech. Dyn. Astron.* **78**(1), 113–123 (2000)
57. Sándor, Z., Érdi, B., Széll, A., Funk, B.: The Relative Lyapunov Indicator: An Efficient Method of Chaos Detection. *Cel. Mech. Dyn. Astron.* **90**(1), 127–138 (2004)
58. Simonsen, I., Hansen, A., Nes O. M.: Determination of the Hurst exponent by use of wavelet transforms. *Phys. Rev. E* **58**(3), 2779–2787 (1998)
59. Skokos, Ch.: Alignment indices: a new, simple method for determining the ordered or chaotic nature of orbits. *J. Phys. A* **34**(47), 10029–10043 (2001)
60. Skokos, Ch., Bountis, T. C., Antonopoulos, Ch.: Geometrical properties of local dynamics in Hamiltonian systems: The Generalized Alignment Index (GALI) method. *Physica D* **231**(1), 30–54 (2007)
61. Skokos, Ch.: The Lyapunov Characteristic Exponents and Their Computation. *Lect. Notes Phys.* **790**, 63–135 (2010)
62. Suyal, V., Prasad, A., Singh H. P.: Nonlinear Time Series Analysis of Sunspot Data. *Sol. Phys.* **260**(2), 441–449 (2009)
63. Szezech, J. D., Schelin, A. B., Caldas, I. L., Lopes, S. R., Morrison, P. J., Viana, R. L.: Finite-time rotation number: A fast indicator for chaotic dynamical structures. *Phys. Lett. A* **377**(6), 452–456 (2013)
64. Tarnopolski, M.: Distinguishing short and long Fermi gamma-ray bursts. *Mont. Not. R. Astron. Soc.* **454**(1), 1132–1139 (2015)
65. Theodoridis, S., Koutroumbas, K.: *Pattern Recognition*. Elsevier Academic Press, 2nd edition (2009)
66. Vandewalle, N., Ausloos, M.: Crossing of two mobile averages: A method for measuring the roughness exponent. *Phys. Rev. E* **58**(5), 6832–6834 (1998)
67. Voglis, N., Contopoulos, G., Efthymiopoulos, C.: Detection of Ordered and Chaotic Motion Using the Dynamical Spectra. *Cel. Mech. Dyn. Astron.* **73**(1–4), 211–220 (1999)
68. Wainwright, J., Ellis, G. F. R.: *Dynamical Systems in Cosmology*. Cambridge University Press (1997)
69. Wang, R., Xiao, D.: Bifurcations and chaotic dynamics in a 4-dimensional competitive LotkaVolterra system. *Nonlinear Dyn.* **59**(3) 411–422 (2010)

-
70. Wolf, A., Swift, J. B., Swinney H. L., Vastano J. A.: Determining Lyapunov Exponents from a Time Series. *Phys. D* **16**(3), 285–317 (1985)
 71. Zhang, X., Zhu, H., Yao, H.: Analysis of a new three-dimensional chaotic system. *Nonlinear Dyn.* **67**(1), 335–443 (2012)
 72. Zotos, E. E., Caranicolas, N. D.: Order and chaos in a new 3D dynamical model describing motion in non-axially symmetric galaxies. *Nonlinear Dyn.* **74**(4), 1203–1221 (2013)
 73. Zotos, E. E.: How does the mass transport in disk galaxy models influence the character of orbits? *Baltic Astron.* **23**, 151–170 (2014)